Single-Breath-Hold 3-D CINE Imaging of the Left Ventricle using Cartesian Sampling

Jens Wetzl[1,2], Michaela Schmidt[3], François Pontana[4],
Benjamin Longère[4], Felix Lugauer[1], Andreas Maier[1,2],
Joachim Hornegger[1,2] and Christoph Forman[3]

Affiliations:

1 Pattern Recognition Lab, Department of Computer Science,
Friedrich-Alexander-Universität Erlangen-Nürnberg, Erlangen, Germany

2 Erlangen Graduate School in Advanced Optical Technologies (SAOT),
Friedrich-Alexander-Universität Erlangen-Nürnberg, Erlangen, Germany

3 Siemens Healthcare GmbH, Erlangen, Germany

4 Department of Cardiovascular Imaging, CHU Lille and Univ. Lille,
F-59000 Lille, France

Notes:

Running Head:	Single-Breath-Hold 3-D CINE Imaging
Correspondence to:	Jens Wetzl,
	Pattern Recognition Lab
	(Department of Computer Science),
	Friedrich-Alexander-Universität Erlangen-Nürnberg,
	Martensstr. 3, D-91058 Erlangen, Germany.
	E-mail: jens.wetzl@fau.de
	Phone: +49 9131 85 27874
	Fax: +49 9131 303811

Word count:

Abstract:	184 words	Figures & Tables:	11
Manuscript:	4000 words	References:	37

ABSTRACT

Object: To evaluate a single-breath-hold approach for Cartesian 3-D CINE imaging of the left ventricle with a nearly isotropic resolution of $1.9 \times 1.9 \times 2.5 \, \mathrm{mm}^3$ and a breath-hold duration of $\sim 19 \, \mathrm{s}$ against a standard stack of 2-D CINE slices acquired in multiple breath-holds. Validation is performed with data sets from 10 healthy volunteers.

Materials and Methods: A Cartesian sampling pattern based on the spiral phyllotaxis and a compressed sensing reconstruction method are proposed to allow 3-D CINE imaging with high acceleration factors. The fully integrated reconstruction uses multiple graphics processing units to speed up the reconstruction. 2-D CINE and 3-D CINE are compared based on ventricular function parameters, contrast-to-noise ratio and edge sharpness measurements.

Results: Visual comparisons of corresponding short-axis slices of 2-D and 3-D CINE show an excellent match, while 3-D CINE also allows reformatting to other orientations. Ventricular function parameters do not significantly differ from values based on 2-D CINE imaging. Reconstruction times are below $4 \, \mathrm{min}$.

Conclusion: We demonstrate single-breath-hold 3-D CINE imaging in volunteers and three example patient cases, which features fast reconstruction and allows reformatting to arbitrary orientations.

Key words: 3-D CINE imaging, compressed sensing, ventricular function

2

INTRODUCTION

CINE magnetic resonance imaging (MRI) allows the assessment of cardiac morphology and function. To determine ventricular function parameters, the current gold standard is a stack of 2-D CINE acquisitions in multiple breath-holds to cover the ventricles. This is suboptimal in several respects. Firstly, multiple breath-holds in quick succession require a high degree of cooperation from patients and may put increased strain on them, which might result in imperfect breath-holding. Secondly, while typical 2-D CINE acquisitions feature a high in-plane resolution, their low slice resolution does not allow retrospective reformatting to arbitrary orientations, e.g. from short-axis to long-axis views.

Based on advancements for accelerating MRI acquisitions, such as parallel imaging [1, 2] and compressed sensing (CS) [3, 4], addressing these limitations has been an ongoing topic of research. On the one hand, certain methods try to reduce patient strain by restricting the acquisition to a single breath-hold. One option is real-time 2-D CINE imaging [5]. The other is 3-D CINE imaging, e.g. based on 3-D "stack-of-spirals" acquisition [6, 7] or Cartesian acquisition [8] using parallel imaging acceleration and 3-D radial "stack-of-stars" acquisition [9] using CS acceleration. The reported length of this breath-hold ranges from 10 to 27 s. However, none of these methods feature a high slice resolution (the reported slice thickness ranges from 3 to 10 mm), so retrospective reformatting is not possible without sacrificing image quality. On the other hand, different methods forgo breath-holding altogether and acquire data during free breathing. Methods for 3-D CINE imaging include a Cartesian-sampled, parallel-imaging-accelerated approach [10], a Cartesian-sampled CS-accelerated approach [11] and one based on radial acquisition [12]. 3-D CINE in the context of congenital heart disease using Cartesian sampling and CS without [13] and with [14] self-gating has been demonstrated in pediatric patients using contrast agent and sedation. Some methods combine 3-D CINE and coronary angiography, either with radial [15] or golden-angle radial acquisition [16]. Another option is to apply a super-resolution technique to multiple 2-D CINE stacks in different orientations to obtain an isotropic 3-D CINE volume [17]. Naturally, these methods have much longer acquisition times to have enough consistent data for reconstruction, with a reported range of 4 to 14 min. Reconstruction times can also be longer, because data inconsistency due to respiratory motion has to be addressed during reconstruction, and in general, because reconstruction of non-Cartesian data is more time-consuming. However, the advantage besides the lack of breath-holding is that most free-breathing methods feature isotropic or nearly isotropic resolution, with reported values ranging from 1.0 to 2.5 mm^3.

We propose a single-breath-hold method for Cartesian 3-D CINE imaging of the left ventricle (LV) with a nearly isotropic measured resolution of $1.9 \times 1.9 \times 2.5$ mm^3 interpolated to $(1.9 \text{ mm})^3$ and a breath-hold duration of ~ 19 s. The method is validated in 10 healthy volunteers and three example patient cases. Additionally, the feasibility of whole-heart (WH) imaging in a single, prolonged breath-hold of ~ 32 s is demonstrated in volunteers. Image reconstruction is fully integrated into the scanner software, using mul-

tiple graphics processing units (GPUs) for fast image calculation to enable reconstruction times of less than 4 min.

MATERIALS AND METHODS

To achieve an acquisition time that fits within a single breath-hold, CS [3, 4] is applied to reduce the number of samples necessary for image reconstruction. Our sampling pattern that guarantees an incoherent sampling of k-space and our non-linear reconstruction incorporating a sparsity constraint in the wavelet domain are described in the following subsections.

Sampling Pattern

Incoherent sampling of the Cartesian phase-encoding plane was achieved by using the spiral phyllotaxis pattern [18], extended for multiple cardiac phases from the formulation in [19]. As the acquisition was prospectively ECG-triggered, the sampling patterns for each cardiac phase could be selected individually. To increase overall k-space coverage, a spiral phyllotaxis pattern with the desired undersampling factor was successively rotated by a fixed angle for each cardiac phase $t \in [1, T]$, with T the number of phases:

$$r_{n,t} = \sqrt{\frac{n}{N}}, \qquad (1) \qquad \varphi_{n,t} = n \cdot \pi \left(3 - \sqrt{5}\right) + t \cdot \varphi_{\text{offset}}, \qquad (2)$$

$$y_{n,t} = r_{n,t}^{v_y} \cdot \cos \varphi_{n,t}, \qquad (3) \qquad z_{n,t} = r_{n,t}^{v_z} \cdot \sin \varphi_{n,t}, \qquad (4)$$

$$v_y = v^{\frac{N_y}{N_y + N_z}}, \qquad (5) \qquad v_z = v^{\frac{N_z}{N_y + N_z}}, \qquad (6)$$

where $(r_{n,t}, \varphi_{n,t})$ are the polar coordinates and $(y_{n,t}, z_{n,t})$ the Cartesian coordinates of sample n out of N total samples for the pattern of cardiac phase t. N is determined by the desired acceleration factor and the size of the field of view. During the conversion to Cartesian coordinates, a variable-density correction is applied using a variable-density factor $v = v_y \cdot v_z$ split into separate factors for phase and partition direction according to the image aspect ratio $\frac{N_y}{N_z}$. Values $\varphi_{\text{offset}} = 12°$ and $v = 0.7$ were empirically selected.

Time-averaged coil sensitivity maps (CSM) were computed with an ESPIRiT approach [20], which requires a fully-sampled rectangular area around the center of k-space. Additionally, to enlarge the fully-sampled area, the pattern as defined by Equations (1)–(6) is further modified by moving duplicate samples to adjacent, unsampled positions (cf. Figure 1). For each k-space position with duplicates, a duplicate is randomly selected and moved to an unsampled position in its 8-neighborhood, i.e., direct neighbors in horizontal, vertical and diagonal direction, if such a position exists. This process is repeated until no more samples can be relocated.
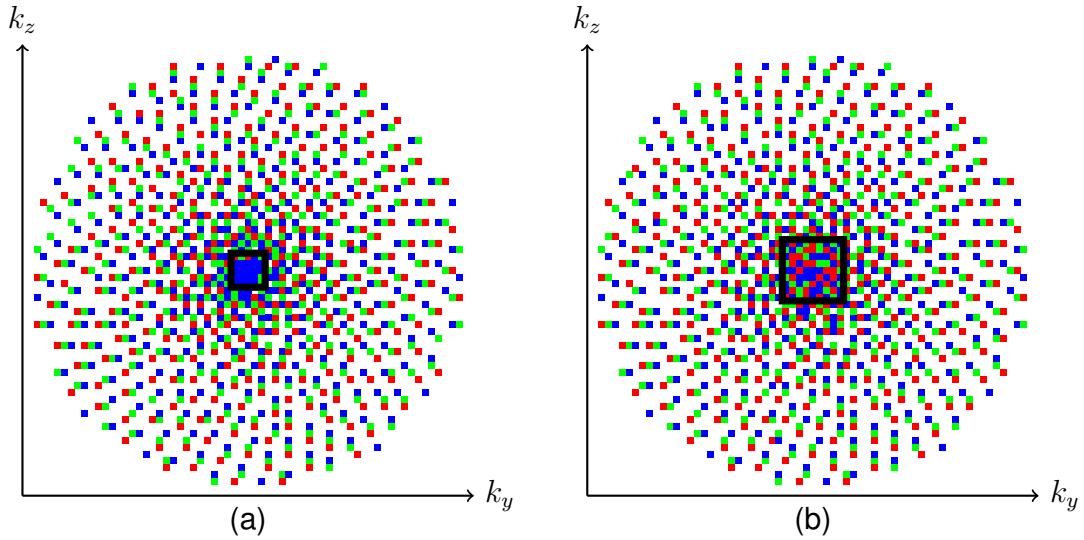
FIG. 1. Rotated phyllotaxis (a) and modified pattern (b) for 3 cardiac phases (red, green, blue). The fully sampled area is outlined in black. The parameters for the pattern are $N_y = N_z = 64$ and $N = 374$, giving an acceleration factor of approximately 11.

Data Reconstruction

For CS reconstruction, we used a non-linear, iterative SENSE approach [1] with spatio-temporal wavelet regularization. The "soft" SENSE method described in [20] was adopted to prevent folding artifacts if the imaged object is larger than the field-of-view. For this purpose, multiple images $\{\boldsymbol{x}_{i,t}\}_{i\in[1,I],\ t\in[1,T]}$, with I the number of coil sensitivity maps per coil and T the number of cardiac phases, are reconstructed as [21, 22]

$$\{\boldsymbol{x}_{i,t}\}_{\substack{i\in[1,I] \\ t\in[1,T]}} = \operatorname*{argmin}_{\{\hat{\boldsymbol{x}}_{i,t}\}} \sum_{i=1}^{I}\sum_{t=1}^{T}\sum_{c=1}^{C} \|\boldsymbol{A}_t\boldsymbol{F}\boldsymbol{S}_{i,c}\hat{\boldsymbol{x}}_{i,t} - \boldsymbol{y}_{t,c}\|_2^2 \qquad (7)$$

$$+\lambda_\sigma \cdot I_{\max} \sum_{i=1}^{I}\sum_{t=1}^{T} \|\boldsymbol{W}_\sigma\hat{\boldsymbol{x}}_{i,t}\|_1$$

$$+\lambda_\tau \cdot I_{\max} \sum_{i=1}^{I} \|\boldsymbol{W}_\tau(\hat{\boldsymbol{x}}_{i,1}^\top,\ldots,\hat{\boldsymbol{x}}_{i,T}^\top)^\top\|_1,$$

where C denotes the number of coils, $\boldsymbol{A}_t$ is the sampling pattern for time t, $\boldsymbol{F}$ is the Fourier transform, $\boldsymbol{S}_{i,c}$ the element-wise multiplication by the ith sensitivity map of coil c, $\boldsymbol{y}_{t,c}$ the measured data for time t and coil c, λ_σ and λ_τ are the spatial and temporal regularization parameters, $\boldsymbol{W}_\sigma$ and $\boldsymbol{W}_\tau$ are spatial and temporal single-level redundant Haar wavelet transforms, and $I_{\max}$ is the maximum image intensity used for scaling the regularization parameters. We set $I = 2$, and only the images corresponding to $i = 1$, i.e., those corresponding to the coil sensitivity maps with the largest eigenvalue, were presented as the result of the reconstruction. The other images were only used during the reconstruction for artifact prevention and then discarded.

To solve equation (7), a FISTA optimization [21] alternated a gradient descent step for the quadratic terms and the evaluation of the proximal operator of the ℓ_1 terms. The solution of the proximal step was computed using a memory-efficient algorithm proposed by Chambolle and Pock [23]. The optimization was implemented on the graphics processing unit (GPU) and also supports the use of multiple GPUs to achieve clinically acceptable reconstruction times. In order to fit all required data into limited GPU memory, the reconstruction was decoupled by performing a Fourier transform along the fully-sampled readout direction. This reduces the 3-D+t reconstruction problem to many 2-D+t reconstructions with a smaller memory requirement, which can be computed in parallel.

Volunteer and Patient Population

3-D CINE imaging was performed in 10 healthy volunteers (3 female and 7 male, age 30 ± 7) and three patients (1 female and 2 male, age 48 ± 26) referred for cardiac MR imaging, who were able to perform the required breath-hold. These patients were referred with different suspected pathologies: intracardiac thrombus for patient 1, ARVD for patient 2 and hypertrophic cardiomyopathy for patient 3. Imaging confirmed the suspicion for patients 1 and 2, but was negative for patient 3. The study was approved by the local Institutional Review Board.

Acquisition

3-D CINE imaging in short-axis (SA) orientation was performed on $1.5\,\mathrm{T}$ clinical MR scanners (MAGNETOM Aera, Siemens Healthcare, Erlangen, Germany). One acquisition covered just the left ventricle (LV) and was performed in volunteers and patients, another covered the whole heart (WH) and was only performed in volunteers. A 3-D volume-selective, prospectively ECG triggered, balanced-SSFP prototype imaging sequence with the following parameters was used: TR = $2.7\,\mathrm{ms}$, TE = $1.2\,\mathrm{ms}$, $\alpha = 38°$, FOV for LV $400\times(272\pm11)\times(111\pm7)\,\mathrm{mm}^3$, FOV for WH $380\times(265\pm10)\times(150\pm8)\,\mathrm{mm}^3$, acquired voxel size for LV $1.9 \times 1.9 \times 2.5\,\mathrm{mm}^3$ interpolated to $(1.9\,\mathrm{mm})^3$, acquired voxel size for WH $1.6 \times 1.9 \times 2.3\,\mathrm{mm}^3$ interpolated to $(1.6\,\mathrm{mm})^3$, temporal resolution 42–48 ms, slice oversampling of 25 %, fixed acceleration factor of 21 for LV and 23 for WH compared to the fully-sampled matrix and a receiver bandwidth of $1045\,\mathrm{Hz/Px}$. Due to the use of prospective ECG triggering, the number of CINE phases varied according to the subject's heart rate, with the range of observed phases between 16–22. Signal reception was performed with 18 anterior and 12 posterior local coil matrix elements. The size of the fully-sampled k-space center area used for CSM calibration varied between 24×24 to 32×32, based on the subject's heart rate. The breath-hold duration was 19 ± 2 heart beats for LV and 33 ± 2 heartbeats for WH. The acquisition time was $19 \pm 5\,\mathrm{s}$ for LV and $32 \pm 7\,\mathrm{s}$ for WH.

For all volunteers, a multi-slice SA 2-D bSSFP CINE acquisition with retrospective gating using $2\times$ accelerated GRAPPA [2] in 5–6 breath-holds was performed to cover the

same volume with a similar temporal resolution, an identical in-plane resolution and a slice thickness of 8 mm. The acquisition time was $2\,\text{min}\,46\,\text{s} \pm 28\,\text{s}$, comprising of $\sim 15\,\text{s}$ breath-holds and breaks of 15 s between subsequent breath-holds. For the patient examples, the reference multi-slice SA 2-D bSSFP CINE acquisitions had a higher in-plane resolution of $(1.1\,\text{mm})^2$ or $(1.6\,\text{mm})^2$, a slice thickness of 8 mm, and a temporal resolution of 32 ms. Late gadolinium enhancement (LGE) imaging was also performed for patient 1 with an in-plane resolution of $(1.6\,\text{mm})^2$ and a slice thickness of 8 mm.

Iterative Reconstruction

The prototype reconstruction was fully integrated on a standard clinical scanner reconstruction system (8-core 2.1 GHz Intel® Xeon® processor, 64 GB RAM, NVIDIA® Tesla™ K10, which comprises two GPUs of type GK104 with 8 GB VRAM).

To determine appropriate parameters for the iterative reconstruction, one volunteer data set was reconstructed with a varying number of iterations (between 1 and 80), and all volunteer data sets were reconstructed with a varying number of spatial regularization factors λ_σ (between 0.0001 and 0.01) and temporal regularization factors λ_τ (between 0.05 and 0.0005). Convergence of the iterative process was determined by monitoring the value of the objective function in equation (7). Visual inspection of the results for different regularization factors by two cardiac MRI experts (6 and 17 years of experience, respectively) was used to pick an appropriate regularization value, which were selected as 20 FISTA iterations, $\lambda_\sigma = 0.001$ and $\lambda_\tau = 0.005$.

Image Quality Assessment

Quantitative assessment of image quality was performed for multiple criteria. Ventricular function (VF) parameters — end-diastolic volume (EDV), end-systolic volume (ESV), and ejection fraction (EF) — were assessed based on reference 2-D CINE acquisitions and 3-D CINE and compared using the root-mean-squared error (RMSE) and Bland-Altman analysis [24]. Specifically, slices in the 3-D CINE stack were selected to correspond to the slices acquired for the 2-D CINE stack. In one dataset, VF parameters computed from a volumetric 3-D segmentation of all slices were compared to those computed from a slice-based segmentation using the same slices acquired for the 2-D CINE stack. The software *syngo*.via (Siemens Healthcare, Erlangen, Germany) was used to perform the evaluation.

The contrast-to-noise ratio (CNR) between blood pool and myocardium was determined by manually segmenting regions of interest (ROIs) in corresponding medial short-axis slices of both reference 2-D CINE and proposed 3-D CINE as

$$\text{CNR} = \frac{|\text{mean}(R_{\text{blood}}) - \text{mean}(R_{\text{myo}})|}{\text{mean}(R_{\text{blood}})}, \tag{8}$$

where R_{blood} and R_{myo} are the sets of image intensities in blood pool and myocardial ROIs, respectively. The mean blood intensity was used in the denominator as opposed to
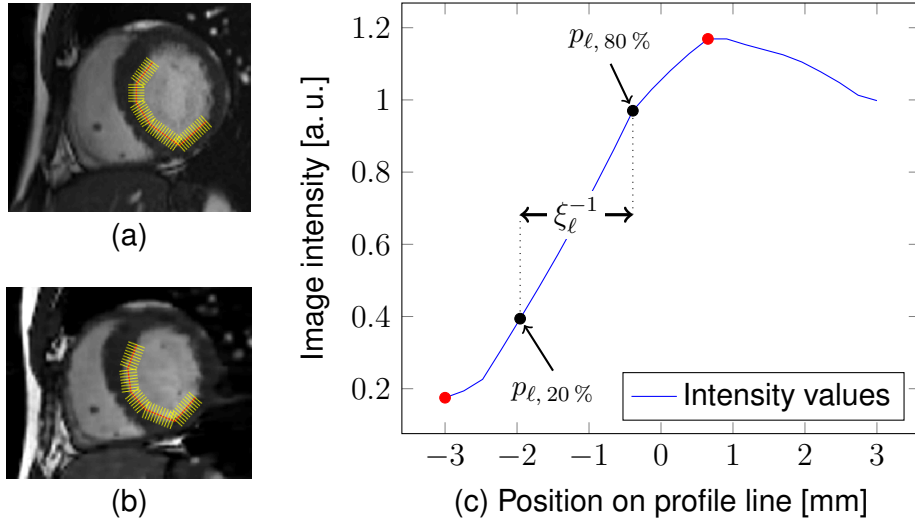
FIG. 2. Edge sharpness computation in corresponding slices of reference 2-D CINE (a) and proposed 3-D CINE (b): After a rough manual segmentation of the edge (red line in a, b), orthogonal profile lines are placed along the edge (yellow lines in a, b), and the inverse of the distance of the 20 % and 80 % points (black dots in c) between the minimum and maximum intensity (red dots in c) along each profile line is computed (c).

its standard deviation to avoid a bias in favor of the CS reconstruction, where denoising may lead to a decreased standard deviation.

The sharpness of the boundary between blood pool and myocardium was compared for the same corresponding slices of 2-D and 3-D CINE used for CNR computation. This comparison was only performed for volunteer data sets, because for the patient examples, the reference 2-D CINE had a much higher spatial resolution than the corresponding 3-D CINE. To determine edge sharpness, the framework according to [25] was used. An initial rough segmentation of the myocardial boundary was performed. Then, orthogonal profile lines ℓ were placed automatically along the boundary. However, the actual edge sharpness measure of [25] was replaced by the more commonly used method suggested in [26–28]. For each profile line, the inverse of the distance of the 20 % and 80 % points between local minimum and maximum was computed, resulting in a value ξ_ℓ with the unit mm^{-1} (see Figure 2):

$$\xi_\ell = \frac{1}{|p_{\ell, 20\%} - p_{\ell, 80\%}|}, \tag{9}$$

where $p_{\ell, 20\%}$ and $p_{\ell, 80\%}$ represent the positions of the 20 % and 80 % points along the ℓth profile line in physical units. The overall edge sharpness value was then chosen as $\xi^* = \text{median}(\xi_1, \ldots, \xi_M)$, where M is the number of profiles.

Statistical significance was determined using paired, two-tailed student's t tests, and values $P < 0.05$ were considered significant.
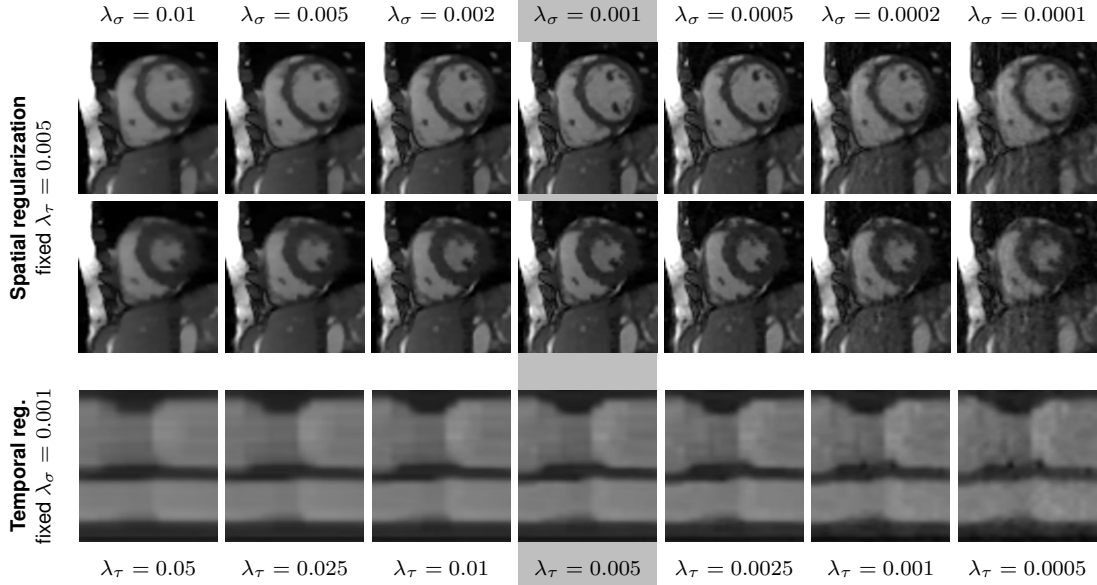
8

FIG. 3. Slices of reconstructions with different spatial regularization parameters λ_σ in end-diastole (top row) and end-systole (middle row) as well as temporal profiles through the left and right ventricle with different temporal regularization parameters λ_τ (bottom row). Chosen spatial and temporal regularization factors are highlighted.

RESULTS

Evaluation of Iterative Reconstruction Parameters

Regarding the convergence of the iterative optimization of Eq. (7), the decrease of the objective function value from 0 to 20 iterations already accounts for $99.5\,\%$ of the decrease from 0 to 80 iterations. A qualitative comparison of reconstructions with different regularization values is shown in Figure 3. The values $\lambda_\sigma = 0.001$ and $\lambda_\tau = 0.005$ were selected by both experts in a majority of cases, 8 out of 10 and 9 out of 10, respectively. In the remaining cases, the experts selected values either one step above or below these values. The average reconstruction time for 3-D CINE was $3\,\mathrm{min}\,29\,\mathrm{s} \pm 34\,\mathrm{s}$ for LV and $8\,\mathrm{min}\,55\,\mathrm{s} \pm 1\,\mathrm{min}$ for WH.

Image Quality Assessment

A qualitative comparison of 2-D CINE and 3-D CINE short-axis image quality as well as reformatted 4-chamber views for 3-D CINE are shown for a volunteer in Figure 4, for patient 1 with an intracardiac thrombus in Figure 5 and for patients 2 and 3 in Figure 6. Figure 4 also shows temporal profiles for 2-D and 3-D CINE to compare the temporal fidelity of the reconstruction. A comparison of LV and WH 3-D CINE for one volunteer is shown in Figure 7.

The RMSE of ventricular function parameters and P values of paired statistical comparisons between 2-D and 3-D CINE images are given in Table 1. Bland-Altman and scatter plots for EDV, ESV and EF are shown in Figure 8.

9

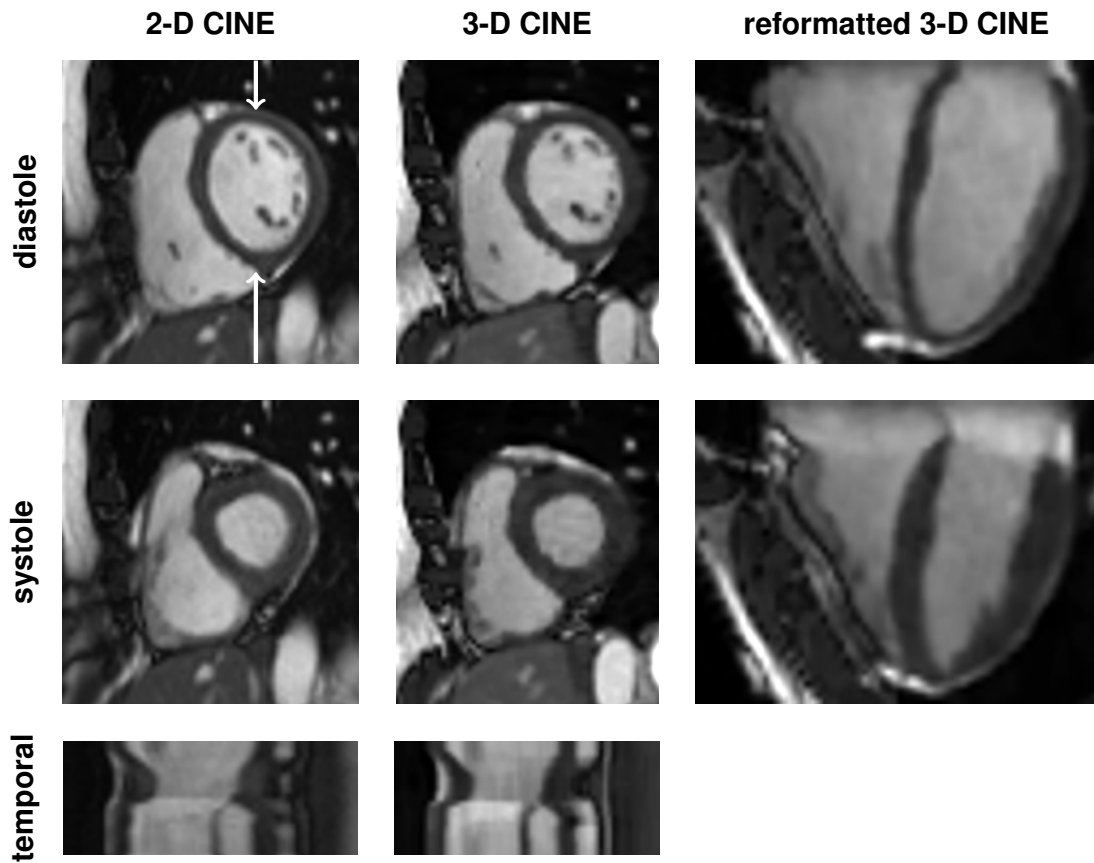| | **2-D CINE** | **3-D CINE** | **reformatted 3-D CINE** |

FIG. 4. Qualitative comparison of corresponding short-axis slices of reference 2-D CINE and proposed 3-D CINE, as well as 3-D CINE reformatted to horizontal long-axis view, in end-diastole and end-systole of a volunteer. Temporal profiles for a line through the largest diameter of the left ventricle (between the white arrows in the diastolic 2-D CINE image) of the same short-axis slices for 2-D and 3-D CINE show the temporal fidelity. We attribute the more pronounced contrast change in the blood pool of the 3-D CINE temporal profile after systole to the inflow effect, which does not influence the contrast of 2-D imaging as strongly.
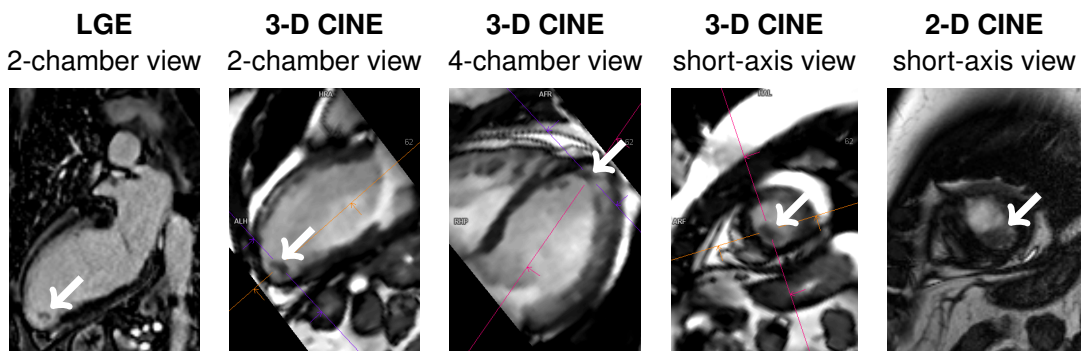

FIG. 5. Patient case 1 with an intracardiac thrombus (white arrows) visualized with late gadolinium enhancement (LGE) imaging in 2-chamber view, 2-D CINE imaging in short-axis view, and with 3-D CINE imaging reformatted to 2-chamber view, 4-chamber view and short-axis view. The in-plane resolution for LGE imaging and 2-D CINE imaging was $(1.6\,\text{mm})^2$ and $(1.1\,\text{mm})^2$, respectively, both with a slice thickness of 8 mm, compared to $1.9 \times 1.9 \times 2.5\,\text{mm}^3$ resolution for 3-D CINE imaging.
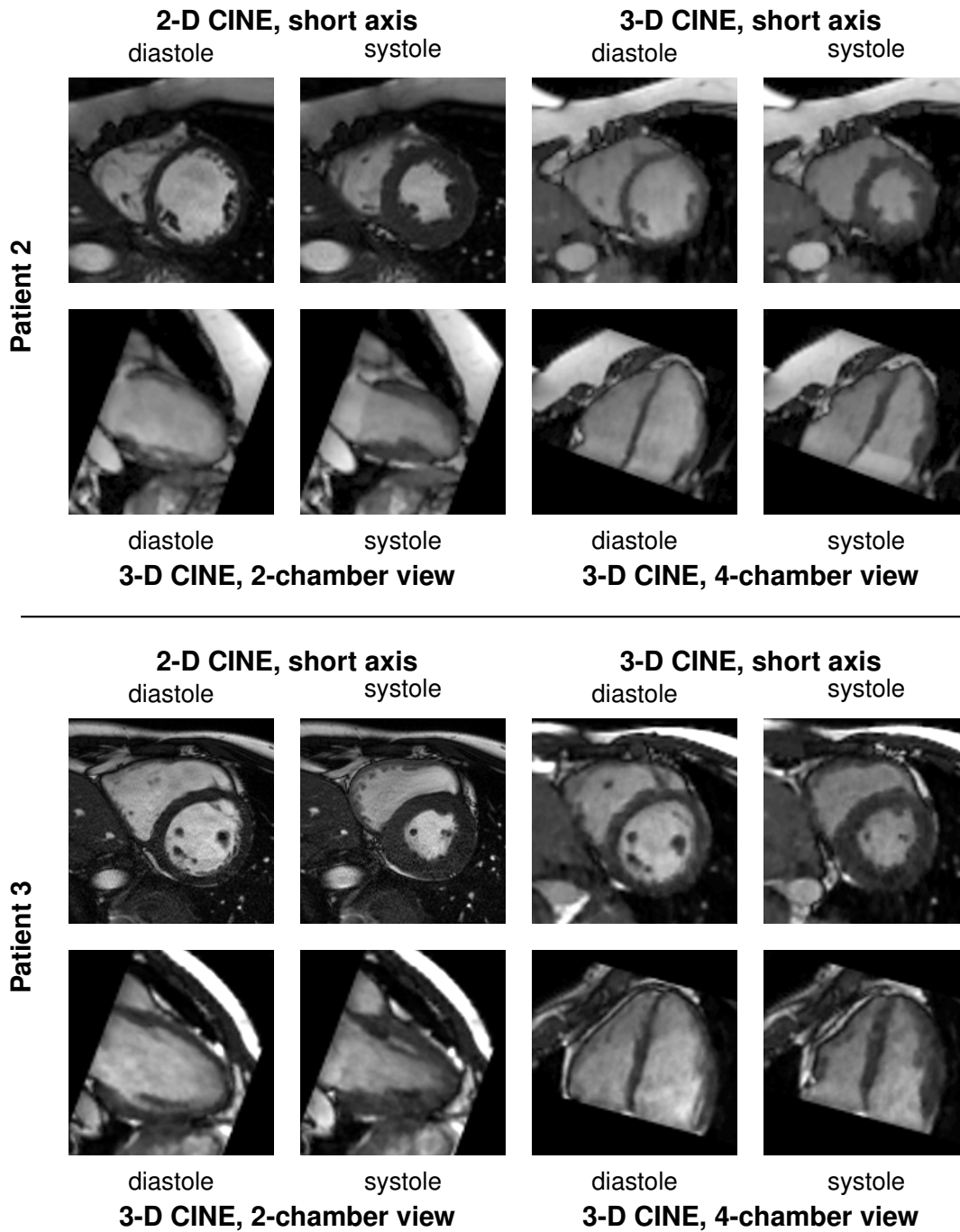
FIG. 6. Qualitative results for patient cases 2 and 3, showing 2-D CINE imaging in short-axis view and 3-D CINE imaging reformatted to 2-chamber view, 4-chamber view and short-axis view. The in-plane resolution for 2-D CINE imaging was $(1.6\,\text{mm})^2$ for patient 2 and $(1.1\,\text{mm})^2$ for patient 3, with a slice thickness of $8\,\text{mm}$, compared to $1.9 \times 1.9 \times 2.5\,\text{mm}^3$ resolution for 3-D CINE imaging.

The meshes obtained from the volumetric and the slice-based segmentation can be seen in Figure 9 to allow a visual comparison. The VF parameters computed from the volumetric segmentation had an EDV that was $14\,\%$ higher, an ESV that was $16\,\%$ higher and an EF that was $2\,\%$ lower than those computed from the slice-based segmentation.
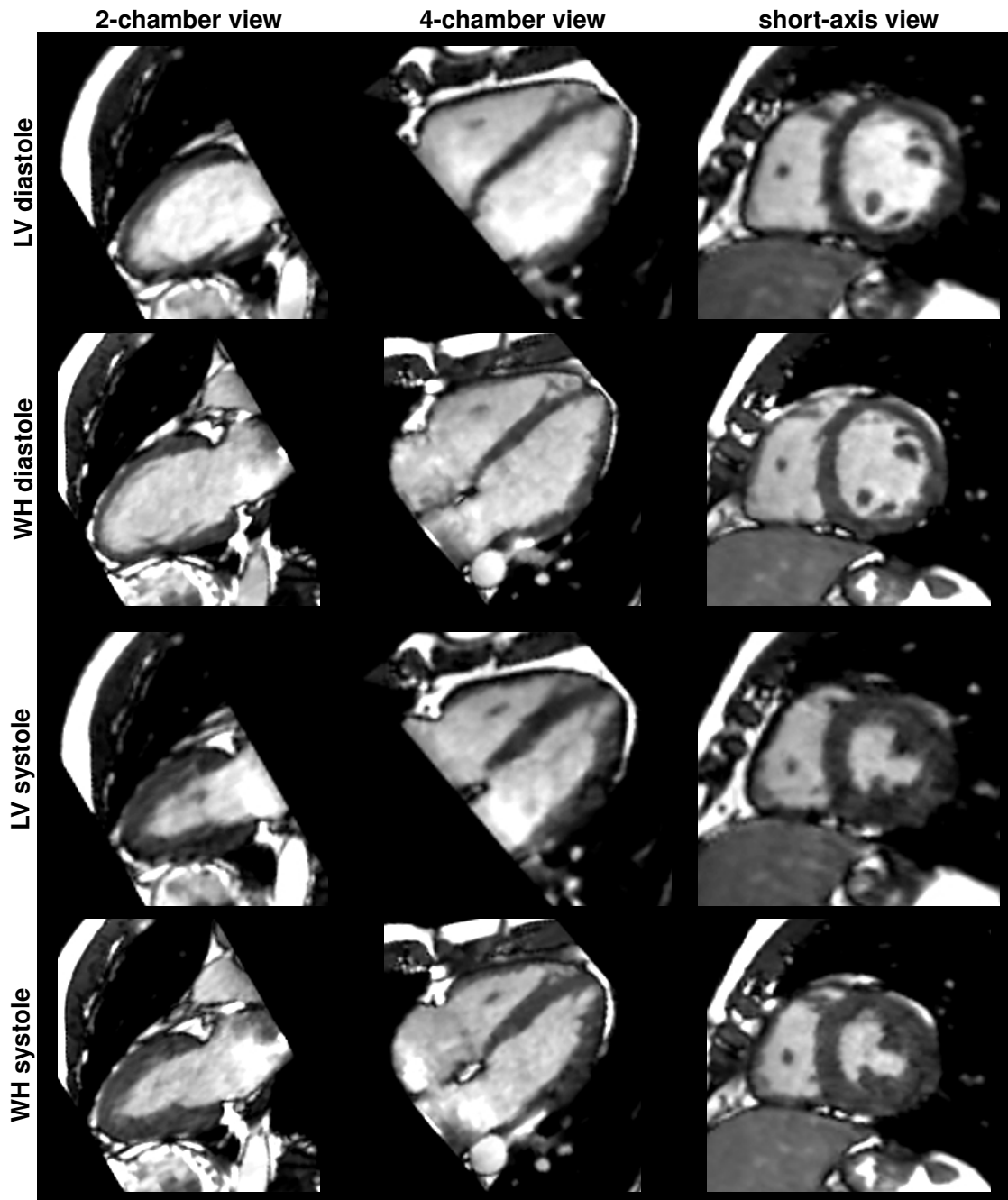
FIG. 7. Qualitative comparison of reformatted 2-chamber view, 4-chamber view and short-axis view orientation for LV (odd rows) and WH (even rows) 3-D CINE in end-diastole (top rows) and end-systole (bottom rows) of a volunteer.

The CNR between blood pool and myocardium was 0.72 ± 0.04 for reference 2-D CINE, 0.70 ± 0.02 for LV 3-D CINE, and 0.60 ± 0.03 for WH 3-D CINE. The difference between LV 3-D CINE and the reference is not statistically significant ($P = 0.12$), while the difference between WH 3-D CINE and the reference is ($P = 0.02$). Box plots for edge sharpness of the boundary between blood pool and myocardium are shown in Figure 10.

	RMSE	P value
End-diastolic volume [mL]	4.4	$P = 0.089$
End-systolic volume [mL]	3.6	$P = 0.630$
Ejection fraction [%]	2.1	$P = 0.088$

Table 1. Root-mean-squared errors of ventricular function parameters for volunteers as well as P values of paired t-tests for parameters computed from 2-D and 3-D CINE images.
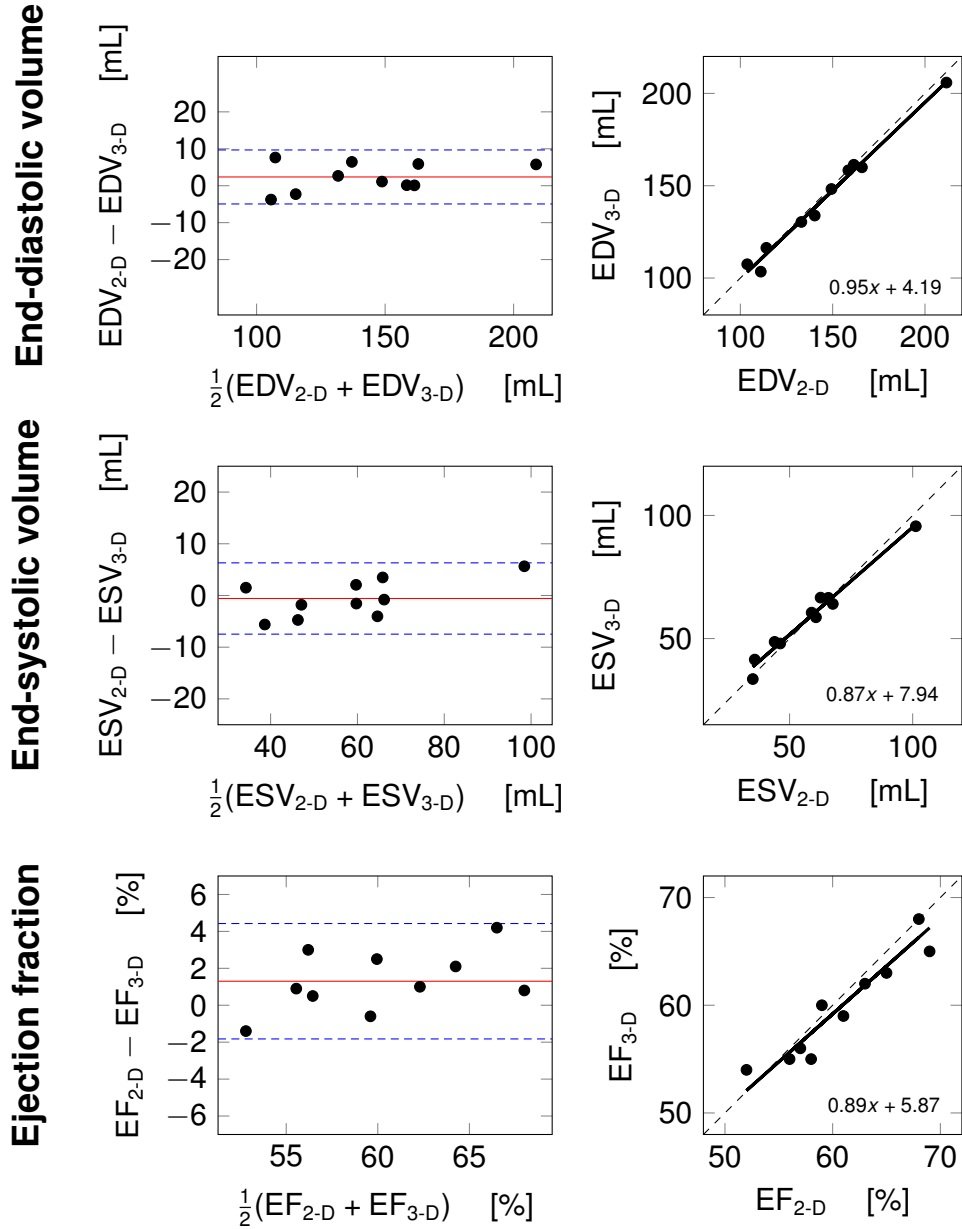

FIG. 8. Bland-Altman plots (left column) and scatter plots (right column) of end-diastolic volume (top row), end-systolic volume (middle row) and ejection fraction (bottom row) for volunteers. In the Bland-Altman plots, the mean differences between 2-D reference and 3-D CINE is denoted in red and the 95 % confidence intervals in blue. In the scatter plots, the dashed lines are the $x = y$ lines, and the solid lines are the linear regression, with their formulae in the bottom right corner.
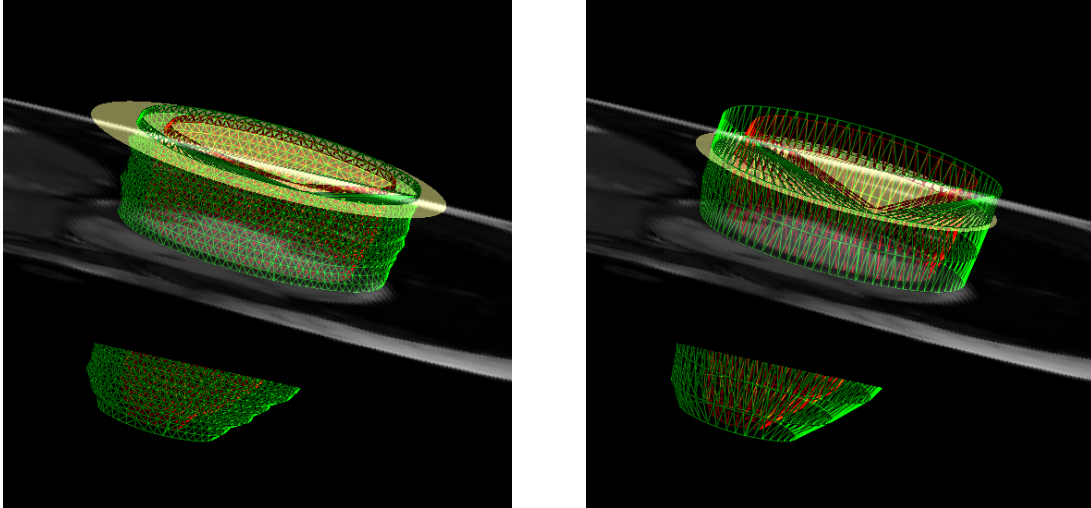
FIG. 9. Segmented end-diastolic epi- (green) and endocardial (red) meshes of the left ventricle based on all slices of a volunteer 3-D CINE volume (left) and only using the slices acquired in the reference 2-D CINE (right).
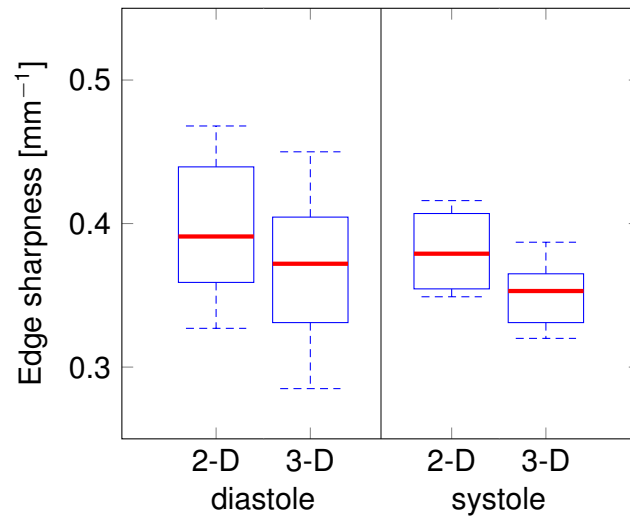

FIG. 10. Box plots of edge sharpness values for volunteers in corresponding short-axis slices for reference 2-D CINE and proposed 3-D CINE in diastole (left side) and systole (right side).

The difference in edge sharpness between 2-D CINE and 3-D CINE is not statistically significant for diastole ($P = 0.06$), but is for systole ($P = 0.001$).

DISCUSSION

Single-breath-hold 3-D CINE imaging was successfully applied in all volunteers and patients who showed the required breath-hold capacity. A volume of the left ventricle with nearly isotropic resolution could be acquired much faster than the gold-standard 2-D CINE stack and reconstructed directly on the scanner in under 4 minutes. An additional feasibility study in volunteers showed the potential for whole-heart imaging with this method in a single, prolonged breath-hold. Due to its nearly isotropic resolution, arbitrary views

14

can be generated from this one acquisition, reducing the effort required to plan multiple views for 2-D CINE imaging. Thus, 3-D CINE may be useful for visualizing complex cardiac anatomy and function, e. g. for the diagnosis of congenital heart defects, or thrombus visualization as seen in Figure 5, in addition to analysis of ventricular function. Due to the use of prospective ECG triggering, we expect the presented method to be applicable in the presence of heart-rate variation during the acquisition, though no major arrhythmia was observed in the volunteer and patient datasets.

The spiral phyllotaxis sampling pattern is well suited for adaptation to multiple cardiac phases by rotation as its mathemetical basis is described in polar space. Other methods for generating sparse sampling patterns directly in Cartesian space, e. g., Poisson disk sampling or patterns based on pseudorandom number sequences like the Niederreither sequence [29], would require more complex alterations to ensure the same favorable properties across cardiac phases that the spiral phyllotaxis pattern does by simple rotation.

Concerning the parameters for iterative reconstruction, observation of decrease of the objective function value suggests that 20 FISTA iterations are sufficient. The agreement of both experts on the selected values for almost all volunteer data sets indicates that it is largely independent of the imaged subject. Thus, while the selection was only based on volunteer data, we believe that it is also a good choice for the patient data sets. L-curve analysis [30] could be used for an objective determination of the regularization parameter, but this automatic selection may not match radiologists' desired image appearance. The reconstruction times of under 4 min for LV and under 10 min for WH are in a clinically relevant range, leveraging multi-GPU acceleration available in current clinical systems. Methods based on non-Cartesian sampling often require reconstruction times in the order of hours [16] without GPU acceleration. While it has been shown that the gridding and re-gridding steps required for reconstruction of non-Cartesian data can be highly accelerated using GPUs [31], they still account for about half of the total reconstruction time. As these steps are not required for the reconstruction of Cartesian data, our approach has an inherent advantage over comparable algorithms for non-Cartesian data. GPU acceleration for total-variation-based filtering commonly used in the iterative reconstruction of radially acquired data has also been demonstrated [32]. As the Cartesian acquisition allows a decoupled reconstruction, slices can be reconstructed independently and could be presented to the MRI operator successively even before the entire volume is reconstructed. Thus, the operator wouldn't need to wait the entire 4 minute reconstruction time in order to determine if the acquisition was successful or not. Coil compression [33] was not used in this study, but holds potential for further reduction of the reconstruction time.

The overall visual impression of volunteer 2-D CINE and 3-D CINE (see Figure 4), which were acquired at the same in-plane resolution, is very similar. The temporal profiles for 2-D and 3-D CINE show that despite temporal regularization, the systolic contraction is well preserved. Compared to the 2-D CINE, the effective (as opposed to the measured) resolution of the 3-D CINE is slightly lower, which can be seen, e. g., in the slightly blurrier

aspect of the papillary muscles. Due to its nearly isotropic resolution, the proposed 3-D CINE has the advantage that it can be reformatted to arbitrary orientations. While a direct comparison between 2-D CINE and 3-D CINE in patient case 1 (see Figure 5) is more difficult due to their different in-plane resolutions, the intracardiac thrombus is visible in both 2-D CINE and the reformatted 3-D CINE. Where 2-D CINE relies on proper slice planning to allow visualization of the thrombus, arbitrary reformats of a single 3-D CINE acquisition guarantee that a view in the proper orientation is available. Qualitative results for patients 2 and 3 in Figure 6 also show a good match between 2-D CINE imaging and 3-D CINE imaging. Figure 7 demonstrates the increased coverage and resolution of WH over LV 3-D CINE in a volunteer. While the extended breath-hold of 33 heartbeats required for this acquisition is currently too long for most patients, this demonstrates the feasibility of this method if the acquisition were further accelerated or performed in free breathing with some form of respiratory gating or motion compensation.

Regarding the evaluation of ventricular function parameters in volunteers, the Bland-Altman plots in Figure 8 show a good match between 3-D CINE and reference 2-D CINE with small confidence intervals. The use of prospective ECG triggering for 3-D CINE compared to retrospective gating for 2-D CINE could explain the slight underestimation of the EDV, as previously described in [5]. The slight overestimation of the ESV may be due to temporal regularization, as the phases around end-systole contain a high degree of motion. As seen in Table 1, the differences between 2-D and 3-D CINE are not statistically significant. An improvement in the CNR, as outlined below, might improve the accuracy of VF parameter assessment. The temporal resolution of the 3-D CINE is at the lower limit of recommended values [34, 35], increasing it could lead to improved results for subjects with fast heart rates.

The 3-D CINE dataset allows the computation of VF parameters in two ways, either by using a slice-based segmentation with the same slices also acquired in the reference 2-D CINE or with a volumetric segmentation using all slices. To allow a fair comparison, the first method was chosen in the experiment comparing the VF parameters of the reference 2-D CINE and the proposed 3-D CINE, i. e., to compare like with like. The experiment comparing VF parameters using both methods on one 3-D CINE dataset shows increased EDV and ESV values when using the volumetric segmentation. One may speculate that results based on the volumetric segmentation are more accurate because more information is available, but in the absence of a volumetric ground truth segmentation, we chose the slice-based segmentation method for the systematic comparison to the available ground truth.

The lower CNR for 3-D CINE compared to 2-D CINE may be due to two factors. Firstly, the individually acquired 2-D slices experience a constant inflow of unsaturated blood along the slice direction. For LV 3-D CINE, this is only the case for basal slices, as seen in the reformatted systolic images in Figures 4 and 5, where the atrial blood pool is brighter compared to the ventricles. This effect can also be seen in the temporal

16

profiles in Figure 4, where the blood pool signal intensity increases when blood from the atria moves into the imaging volume after systole. While for LV 3-D CINE, the difference in CNR compared to 2-D CINE is not significant yet, it is for WH 3-D CINE, because the atria and parts of the large vessels are included in the imaging volume. Secondly, the maximal possible flip angle within specific-absorption-rate limitations is intrinsically lower for 3-D acquisitions compared to 2-D. However, the contrast still seems sufficient for ventricular function analysis. An improvement could be achieved by interleaving T_2 preparation pulses into the acquisition, as demonstrated in [16].

In terms of edge sharpness, the CS approach for LV 3-D CINE shows no significant loss compared to the GRAPPA-based 2-D CINE acquisition in diastole, but does in systole. The lower systolic edge sharpness for 3-D CINE compared to 2-D CINE (see Figure 10) could be due to temporal regularization, necessary because of the high undersampling factor.

Naturally, the presented method requires the subject's capacity for good breath-holding. If this is given, the presented approach can deliver a volume of the left ventricle with nearly isotropic resolution in a shorter acquisition time than a stack of 2-D CINE slices requiring multiple, albeit shorter, breath-holds. Several possibilities for reducing the 3-D CINE breath-hold time even further could be considered. If the intended application allows it, reducing spatial or temporal resolution is the most straightforward solution. Otherwise, the acceleration factor could be increased by using more sophisticated reconstruction techniques, e. g., by using dictionary learning in the sparsifying transform to deal more effectively with undersampling artifacts from the higher acceleration [36]. However, such a method would also imply longer reconstruction times. Alternatively, one might consider reducing the in-plane resolution and increasing the slice resolution to achieve a fully isotropic resolution for the same acquisition time. However, as the primary goal was the computation of VF parameters and it has been shown previously that decreased in-plane resolution leads to biased VF parameters [37], we favored an in-plane resolution below $(2\,\mathrm{mm})^2$ over a fully isotropic, but lower resolution. While whole-heart acquisition is possible, as demonstrated in our volunteer experiment, the required breath-hold is too long for clinical applicability. Ultimately, a shorter breath-hold in the range of 12–15 s or free-breathing acquisition is preferable for patients incapable of breath-holding or for whole-heart coverage, at the cost of a longer acquisition time. A free-breathing acquisition would also allow a higher spatial and temporal resolution if this is required for the intended application.

CONCLUSION

We have presented a method for single-breath-hold, high-resolution 3-D CINE imaging of the left ventricle, validated in both volunteers and shown exemplarily in three patients. To our knowledge, this is the first report of a single-breath-hold acquisition with a com-

paratively high, nearly isotropic resolution. Additionally, whole-heart 3-D CINE imaging in a prolonged breath-hold was demonstrated in volunteers. Due to its nearly isotropic resolution, 3-D CINE imaging enables retrospective reformatting to arbitrary orientations. Image reconstruction was fully integrated into the scanner software, with multi-GPU support to achieve reconstruction times of less than 4 minutes.

Authors' contributions: Jens Wetzl: protocol and project development, data collection and analysis. Michaela Schmidt: protocol development, data collection and analysis. François Pontana: data collection and analysis. Benjamin Longère: data collection and analysis. Felix Lugauer: data collection and management. Andreas Maier: project development. Joachim Hornegger: project development. Christoph Forman: protocol and project development, data collection and analysis.

Conflict of interest: Jens Wetzl and Felix Lugauer receive project funding from Siemens Healthcare GmbH. Michaela Schmidt and Christoph Forman are employees of Siemens Healthcare GmbH. François Pontana receives research support from Siemens Healthcare GmbH.

Ethical approval: All procedures performed in studies involving human participants were in accordance with the ethical standards of the institutional and/or national research committee and with the 1964 Helsinki declaration and its later amendments or comparable ethical standards.

Informed consent: Informed consent was obtained from all individual participants included in the study.

REFERENCES

1. Pruessmann KP, Weiger M, Scheidegger MB, Boesiger P (1999) SENSE: sensitivity encoding for fast MRI. Magn Reson Med 42(5):952–62

2. Griswold MA, Jakob PM, Heidemann RM, Nittka M, Jellus V, Wang J, Kiefer B, Haase A (2002) Generalized autocalibrating partially parallel acquisitions (GRAPPA). Magn Reson Med 47(6):1202–1210

3. Lustig M, Donoho D, Pauly JM (2007) Sparse MRI: The application of compressed sensing for rapid MR imaging. Magn Reson Med 58(6):1182–95

4. Lustig M, Donoho DL, Santos JM, Pauly JM (2008) Compressed Sensing MRI. IEEE Signal Process Mag 25(2):72–82

5. Vincenti G, Monney P, Chaptinel J, Rutz T, Coppo S, Zenge MO, Schmidt M, Nadar MS, Piccini D, Chèvre P, Stuber M, Schwitter J (2014) Compressed Sensing Single-Breath-Hold CMR for Fast Quantification of LV Function, Volumes, and Mass. JACC Cardiovasc Imaging 7(9):882–892

6. Kressler B, Spincemaille P, Nguyen TD, Cheng L, Xi Hai Z, Prince MR, Wang Y (2007) Three-dimensional cine imaging using variable-density spiral trajectories and SSFP with application to coronary artery angiography. Magn Reson Med 58(3):535–543

7. Barkauskas KJ, Rajiah P, Ashwath R, Hamilton JI, Chen Y, Ma D, Wright KL, Gulani V, Griswold MA, Seiberlich N (2014) Quantification of left ventricular functional parameter values using 3D spiral bSSFP and through-time Non-Cartesian GRAPPA. J Cardiovasc Magn Reson 16:65

8. Makowski MR, Wiethoff AJ, Jansen CH, Uribe S, Parish V, Schuster A, Botnar RM, Bell A, Kiesewetter C, Razavi R, Schaeffter T, Greil GF (2012) Single breath-hold assessment of cardiac function using an accelerated 3D single breath-hold acquisition technique - comparison of an intravascular and extravascular contrast agent. J Cardiovasc Magn Reson 14:53

9. Wech T, Pickl W, Tran-Gia J, Ritter C, Beer M, Hahn D, Köstler H (2014) Whole-Heart Cine MRI in a Single Breath-Hold – A Compressed Sensing Accelerated 3D Acquisition Technique for Assessment of Cardiac Function. Fortschr Röntgenstrahlung 186:37–41

10. Uribe S, Muthurangu V, Boubertakh R, Schaeffter T, Razavi R, Hill DL, Hansen MS (2007) Whole-heart cine MRI using real-time respiratory self-gating. Magn Reson Med 57(3):606–613

11. Usman M, Ruijsink B, Nazir M, Cruz G, Prieto C (2016) Free breathing whole-heart 3D CINE MRI with self-gated Cartesian trajectory. Magn Reson Imaging 38:129–137

12. Liu J, Spincemaille P, Codella NCF, Nguyen TD, Prince MR, Wang Y (2010) Respiratory and cardiac self-gated free-breathing cardiac CINE imaging with multiecho 3D hybrid radial SSFP acquisition. Magn Reson Med 63(5):1230–1237

13. Han F, Rapacchi S, Khan S, Ayad I, Salusky I, Gabriel S, Plotnik A, Finn JP, Hu P (2015) Four-dimensional, multiphase, steady-state imaging with contrast enhancement (MUSIC) in the heart: A feasibility study in children. Magn Reson Med 74(4):1042–1049

14. Han F, Zhou Z, Han E, Gao Y, Nguyen KL, Finn JP, Hu P (2016) Self-gated 4D multi-phase, steady-state imaging with contrast enhancement (MUSIC) using rotating cartesian K-space (ROCK): Validation in children with congenital heart disease. Magn Reson Med , doi: 10.1002/mrm.26376

15. Pang J, Sharif B, Fan Z, Bi X, Arsanjani R, Berman DS, Li D (2014) ECG and navigator-free four-dimensional whole-heart coronary MRA for simultaneous visualization of cardiac anatomy and function. Magn Reson Med 72(5):1208–1217

16. Coppo S, Piccini D, Bonanno G, Chaptinel J, Vincenti G, Feliciano H, van Heeswijk RB, Schwitter J, Stuber M (2015) Free-running 4D whole-heart self-navigated golden angle MRI: Initial results. Magn Reson Med 74(5):1306–1316

17. Odille F, Bustin A, Chen B, Vuissoz PA, Felblinger J (2015) Motion-Corrected, Super-Resolution Reconstruction for High-Resolution 3D Cardiac Cine MRI. In: Navab N, Hornegger J, Wells MW, Frangi FA, eds., Medical Image Computing and Computer-Assisted Intervention – MICCAI 2015: 18th International Conference, Munich, Germany, October 5-9, 2015, Proceedings, Part III,, pp 435–442. Springer International Publishing

18. Vogel H (1979) A better way to construct the sunflower head. Math Biosci 44(3-4):179–189

19. Forman C, Piccini D, Grimm R, Hutter J, Hornegger J, Zenge MO (2014) High-resolution 3D whole-heart coronary MRA: a study on the combination of data acquisition in multiple breath-holds and 1D residual respiratory motion compensation. Magn Reson Mater Phys Biol Med 27(5):435–443

20. Uecker M, Lai P, Murphy MJ, Virtue P, Elad M, Pauly JM, Vasanawala SS, Lustig M (2014) ESPIRiT - an eigenvalue approach to autocalibrating parallel MRI: where SENSE meets GRAPPA. Magn Reson Med 71(3):990–1001

21. Liu J, Rapin J, Chang T, Lefebvre A, Zenge M, Mueller E, Nadar MS (2012) Dynamic cardiac MRI reconstruction with weighted redundant Haar wavelets. In: Proceedings of the 20th scientific meeting, International Society for Magnetic Resonance in Medicine, Melbourne, p 178

22. Wetzl J, Schmidt M, Zenge M, Lugauer F, Lazar L, Nadar MS, Maier A, Hornegger J, Forman C (2015) Isotropic 3-D CINE Imaging with Sub-2mm Resolution in a Single Breath-Hold. In: Proceedings of the 23rd scientific meeting, International Society for Magnetic Resonance in Medicine, Toronto, p 1011

23. Chambolle A, Pock T (2010) A First-Order Primal-Dual Algorithm for Convex Problems with Applications to Imaging. J Math Imaging Vis 40(1):120–145

24. Bland JM, Altman DG (1986) Statistical Methods For Assessing Agreement Between Two Methods Of Clinical Measurement. The Lancet 327(8476):307–310

25. Taubmann O, Wetzl J, Lauritsch G, Maier A, Hornegger J (2015) Sharp as a Tack. In: Handels H, Deserno TM, Meinzer HP, Tolxdorff T, eds., Bildverarbeitung für die Medizin 2015, Informatik aktuell, pp 425–430. Springer Berlin Heidelberg. URL `http://dx.doi.org/10.1007/978-3-662-46224-9{_}73`. Doi 10.1007/978-3-662-46224-9_73

26. Shea SM, Kroeker RM, Deshpande V, Laub G, Zheng J, Finn JP, Li D (2001) Coronary artery imaging: 3D segmented k-space data acquisition with multiple breath-holds and real-time slab following. J Magn Reson Imaging 13(2):301–307

27. Li D, Carr JC, Shea SM, Zheng J, Deshpande VS, Wielopolski PA, Finn JP (2001) Coronary Arteries: Magnetization-prepared Contrast-enhanced Three-dimensional Volume-targeted Breath-hold MR Angiography. Radiology 219(1):270–277. PMID: 11274569

28. Larson AC, Kellman P, Arai A, Hirsch GA, McVeigh E, Li D, Simonetti OP (2005) Preliminary investigation of respiratory self-gating for free-breathing segmented cine MRI. Magn Reson Med 53(1):159–168

29. Niederreither H (1988) Low-Discrepancy and Low-Dispersion Sequences. Number Theory 30:51–70

30. Hansen P (2000) The L-curve and its use in the numerical treatment of inverse problems. WIT Press

31. Nam S, Akçakaya M, Basha T, Stehning C, Manning WJ, Tarokh V, Nezafat R (2013) Compressed sensing reconstruction for whole-heart imaging with 3D radial trajectories: A graphics processing unit implementation. Magn Reson Med 69(1):91–102

32. Knoll F, Unger M, Diwoky C, Clason C, Pock T, Stollberger R (2010) Fast reduction of undersampling artifacts in radial MR angiography with 3D total variation on graphics hardware. Magn Reson Mater Phys Biol Med 23(2):103–114

33. Zhang T, Pauly JM, Vasanawala SS, Lustig M (2013) Coil compression for accelerated imaging with Cartesian sampling. Magn Reson Med 69(2):571–582

34. Kramer CM, Barkhausen J, Flamm SD, Kim RJ, Nagel E (2008) Standardized cardiovascular magnetic resonance imaging (CMR) protocols, society for cardiovascular magnetic resonance: board of trustees task force on standardized protocols. J Cardiovasc Magn Reson 10(1):1–10

35. Kramer CM, Barkhausen J, Flamm SD, Kim RJ, Nagel E (2013) Standardized cardiovascular magnetic resonance (CMR) protocols 2013 update. J Cardiovasc Magn Reson 15(1):1–10

36. Wang Y, Ying L (2014) Compressed Sensing Dynamic Cardiac Cine MRI Using Learned Spatiotemporal Dictionary. IEEE Trans Biomed Eng 61(4):1109–1120

37. Kunz RP, Oellig F, Krummenauer F, Oberholzer K, Romaneehsen B, Vomweg TW, Horstick G, Hayes C, Thelen M, Kreitner KF (2005) Assessment of left ventricular function by breath-hold cine MR imaging: Comparison of different steady-state free precession sequences. Magn Reson Imaging 21(2):140–148